Hydrodynamically bound states of a pair of microrollers: A dynamical system insight

Blaise Delmotte*
LadHyX, UMR CNRS 7646, École Polytechnique, 91128 Palaiseau CEDEX, France

(Received 26 November 2018; published 5 April 2019)

Recent work has identified persistent cluster states which were shown to be assembled and held together by hydrodynamic interactions alone [Driscoll *et al.* Nat. Phys. **13**, 375 (2017)]. These states were seen in systems of colloidal microrollers; microrollers are colloidal particles which rotate about an axis parallel to the floor and generate strong, slowly decaying, advective flows. To understand these bound states, we study a simple, yet rich, model system of two microrollers. Here we show that pairs of microrollers can exhibit hydrodynamic bound states whose nature depends on a dimensionless number, denoted B, that compares the relative strength of gravitational forces and external torques. Using a dynamical system framework, we characterize these various states in phase space and analyze the bifurcations of the system as B varies. In particular, we show that there is a critical value, B^*, above which active flows can beat gravity and lead to stable motile orbiting, or "leapfrog," trajectories, reminiscent of the self-assembled motile structures, called "critters," observed by Driscoll *et al.* We identify the conditions for the emergence of these trajectories and study their basin of attraction. This work shows that a wide variety of stable bound states can be obtained with only two particles. Our results aid in understanding the mechanisms that lead to spontaneous self-assembly in hydrodynamic systems, such as microroller suspensions, as well as how to optimize these systems for particle transport.

DOI: 10.1103/PhysRevFluids.4.044302

I. INTRODUCTION

Synchronization [1,2] and collective motion [3–5] are well documented in the literature on active and driven suspensions at low Reynolds number. The strong, slowly decaying, flow fields induced by the motion of small objects immersed in a viscous fluid play a predominant role in the emergence of coherent structures. Turbulent-like flows in bacteria and sperm suspensions [6–9] and phase synchronization between flagella [10] are illustrative examples in natural systems. Colloidal particles have been designed to mimic the behavior of natural systems at both the individual and collective levels [11,12] and also to explore alternative ways to mix the surrounding fluid or to transport particles at low Reynolds number [13–15]. In particular, recent experiments and simulations have shown that suspensions of torque-driven particles above a floor could self-assemble into stable motile structures, called "critters," that have no analog in natural systems [16]; see Fig. 1. While it is clear that long-ranged hydrodynamics play a leading role in this phenomenon, the conditions for this spontaneous self-assembly must be identified.

The physics of torque-driven colloidal particles (called microrotors) have recently attracted significant attention [13,15,17]. Microrotors can be driven with an external rotating magnetic field [16,18], or by using a Quincke-like instability under the action of an electric [19] or magnetic field

*blaise.delmotte@ladhyx.polytechnique.fr

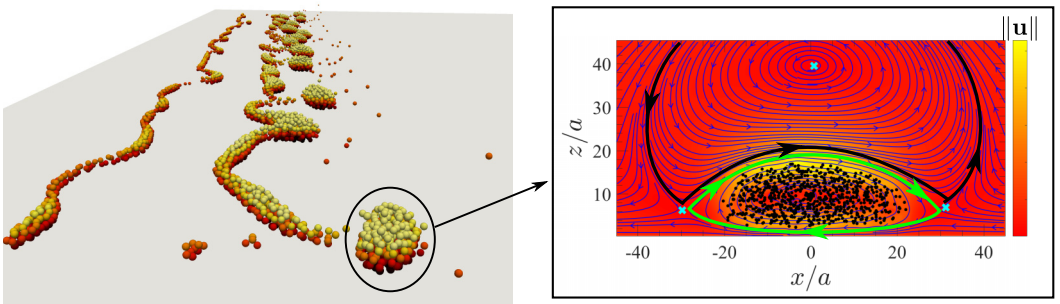

FIG. 1. Left: Detachment of self-sustained motile clusters made of hundreds of microrollers, called critters. Particles are colored according to their translational speed. Right: Cross section of the flow field in the frame of a moving critter in the xz plane. Black circles correspond the particles in the critter. Cyan crosses are stagnation points of the flow. The green line with arrows delimits the recirculation zone where the particles perform a treadmilling motion. The black line with arrows indicates the counter-rotating recirculating flow above the critter. Colorbar is magnitude of the flow field.

[20]. Despite their apparent simplicity, microrotors can lead to complex and interesting dynamics at the collective level. Microrotors can be divided into two categories: (1) microspinners, which rotate in the absence of boundary or with an axis of rotation perpendicular to the interface, and (2) microrollers, which rotate about an axis parallel to the boundary (without necessarily touching it) and thus translate due to the asymmetric stress distribution on their surface. Previous studies have shown that microspinners can phase separate [21], mix the surrounding medium [22], and arrange into large-scale rotating structures [13,20]. In proximity to the floor, suspensions of microrollers form traveling waves [19,23] and shocks [16,23] that can destabilize into finger-like structures whose dense tips detach and self-assemble into stable motile clusters, called critters [16] (cf. Fig. 1). While the hydrodynamic mechanisms for the shock formation and fingering instability are well understood [23,24], the conditions for the detachment of fingertips and their self-assembly into stable motile structures are not well identified. From a dynamical systems point of view, these critters could be viewed as an attractor whose existence and basin of attraction depend on the parameters of the system. Our goal here is to find the relevant parameters of the system to identify the conditions for the existence and stability of such hydrodynamic bound states.

Hydrodynamic bound states of active particles have been observed in various forms [1,17,25]. At the individual level, sperm cells and bacteria swim in circles near boundaries [26–28], while biflagellate microorganisms and other model swimmers can be trapped [29–31] or perform periodic vertical motion [32–35]. At the collective level, Martinez-Pedrero *et al.* [36] showed that the lateral flows generated by heavy microrollers can form horizontal one-dimensional arrays of aligned particles.

Here we propose a dynamical systems approach to study the motion of pairs of microrollers in a viscous fluid, i.e., at low Reynolds number. The dynamics of coplanar neutrally buoyant point microspinners (rotlets) in an unbounded fluid has been studied theoretically [37–39]. A rotlet in an unbounded fluid generates an axisymmetric flow field decaying as $\sim 1/r^2$ [see Fig. 2(a)]. Due to the rotational symmetry of the system, two corotating particles with the same torque, τ, always exhibit neutrally stable periodic trajectories regardless of their separation distance, r. The rotation period of these trajectories, T_R, can be computed analytically and is given by

$$T_R = \frac{16\pi\eta r^3}{\tau}, \tag{1}$$

where η is the dynamic viscosity of the suspending fluid, and τ is the magnitude of the torque applied to the corotating particles. When a no-slip boundary is added to the system, the rotational

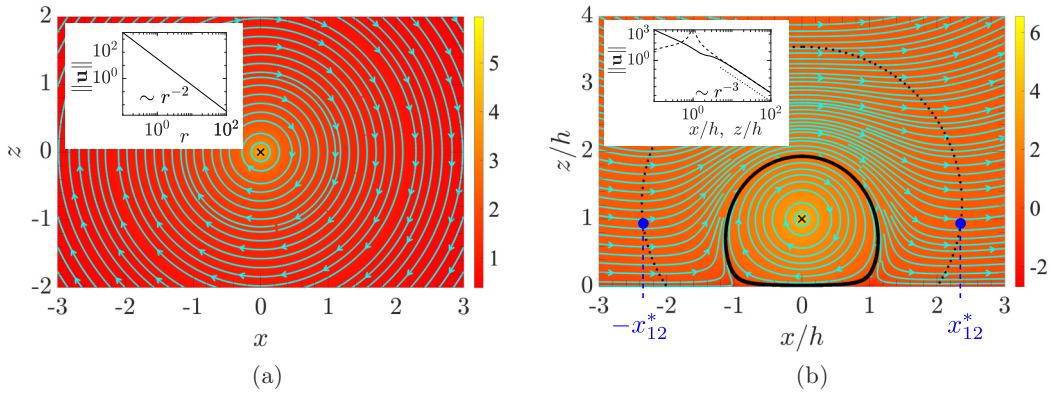

FIG. 2. Flow field **u** around a point torque (rotlet), (a) in an unbounded fluid and (b) in a half-space bounded by a no-slip wall. The decay of the flow fields is provided in the insets. The inset in panel (b) shows the flow magnitude along the x direction at $z = h$ (solid line) and along the z direction at $x = 0$ (dashed line). Cross, location of the rotlet; cyan lines, streamlines; colorbar, $\log|\mathbf{u}|$. The thick line in panel (b) delimits the region of closed streamlines, while the dotted line indicates the contour $u_z = 0$. x_{12}^* is the separation distance where $u_z = 0$ at $z/h = 1$.

symmetry is broken. The decay of the flow field is asymmetric and scales as r^{-3} in the far field [see inset of Fig. 2(b)]. In addition, the presence of the wall divides the flow around a rotlet into two regions: a recirculating region with closed streamlines around the particle, and another with open streamlines [see Fig. 2(b)]. The size of this recirculating region, in the vertical plane that contains the rotlet center, scales linearly with the height above the floor h (perimeter $\approx 7.1h$, area $\approx 3.7h^2$).

Given the qualitatively different flow field induced by the wall, can we then expect to observe periodic states as in the unbounded case? And, if so, under which conditions? In a more realistic case, how do gravity and finite particle size affect the dynamics of the system?

A description and the governing equations of the dynamical system is given in Sec. II. We consider both a simple far-field model using rotlets, as well as a more realistic model that includes gravity, the finite size of the particles and steric repulsion. We study the equilibrium configurations of these systems and their stability in Sec. III. In particular we identify the conditions for the emergence of periodic "leapfrog" trajectories, reminiscent of the particle motion observed in the critters. Finally, we conclude and discuss how these results may be extended to study the dynamics of a large collection of microrollers at the continuum level in Sec. IV.

II. DESCRIPTION OF THE DYNAMICAL SYSTEM

A. System and equations of motion

We consider two spherical particles, with radius a, mass m, and coordinates (x_i, y_i, z_i), $i = 1, 2$, where $y_1 = y_2$, above a no-slip boundary located at $z = 0$. Each particle is subject to an external torque $\tau = \tau_1 = \tau_2$ along the y axis. External forces in the xz plane are written as 2×1 vectors:

$$\mathbf{F}_i = \begin{bmatrix} F_{p,i}^x \\ F_{p,i}^z + F_{g,i} + F_{w,i} \end{bmatrix}, \quad i = 1, 2, \tag{2}$$

where $\mathbf{F}_p$ is the interparticle contact force, F_w is the particle-wall contact force, and F_g is the gravitational force. Vector components are indicated with superscript Latin letters (x or z). Since the particles are coplanar, their transverse velocity (in the y direction) is zero. See Fig. 3(a) for a sketch of the system.

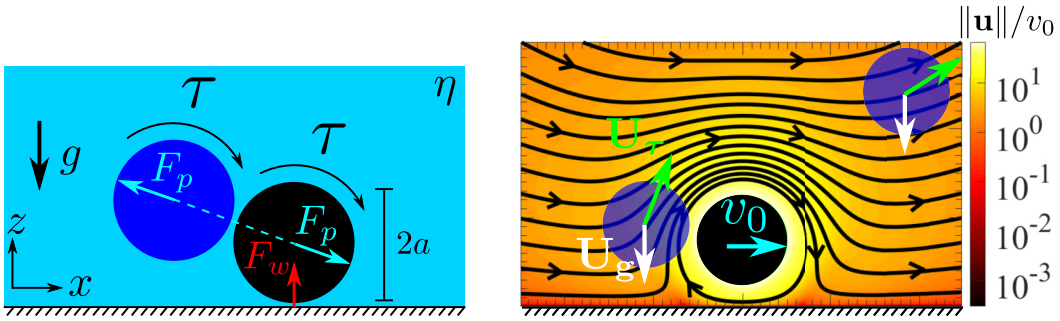

FIG. 3. (a) Schematic of the system: two particles with radius a rotate under the action of an external torque τ in a viscous fluid with viscosity η. They are subject to gravity and interparticle (F_p) and particle-wall (F_w) contact forces. (b) Flow field around a torque driven a particle of radius a normalized by the self-induced velocity v_0, obtained with a high-accuracy numerical method [16,40]. Blue particles represent two different situations where torque-driven flows can counterbalance or beat gravity to lead to a hydrodynamic bound state. U_g is the self-induced velocity due to gravity, and U_τ is the velocity induced by the torque acting on the black particle.

Using the translational invariance of the system along the x axis, one can write the reduced equations of motion for the state vector $\mathbf{x} = (x_{12}, z_{12}, z_C)$:

$$\dot{\mathbf{x}} = \begin{bmatrix} \dot{x}_{12} \\ \dot{z}_{12} \\ \dot{z}_C \end{bmatrix} = \frac{\tau}{\eta}\boldsymbol{\mu}^{U\tau} + \frac{1}{\eta}\mathbf{M}^{UF} \cdot \begin{bmatrix} \mathbf{F}_1 \\ \mathbf{F}_2 \end{bmatrix} = \mathcal{G}(\mathbf{x}), \tag{3}$$

where $x_{12} = x_1 - x_2$, $z_{12} = z_1 - z_2$ are the relative positions, and $z_C = (z_1 + z_2)/2$ is the height of the center of mass. $\boldsymbol{\mu}^{U\tau}$ is a 3×1 vector of scalar mobility functions that relate the torque applied on the particles along the y axis, τ, to the translational speed of the system $\dot{\mathbf{x}}$. $\mathbf{M}^{UF}$ is the 3×4 mobility matrix that relates the forces applied on the particles $\mathbf{F}_i$ to the translational speed of the system $\dot{\mathbf{x}}$. $\boldsymbol{\mu}^{U\tau}$ and $\mathbf{M}^{UF}$ contain the self-induced effects as well as hydrodynamic interactions between the particles. These functions depend exclusively on the geometric parameters of the system: $\mathbf{x}$ and a. The RHS of Eq. (3), $\mathcal{G}(\mathbf{x})$, can be seen as a vector field that depends on the state vector $\mathbf{x}$.

B. Far-field approximation: Rotlets

In the far field limit, i.e., when the particles are far apart from each other and far form the floor, the particles can be modeled as point torques ($a = 0$), called rotlets. Using the rotlet image system above a no-slip boundary from Blake and Chwang [41], we derive simple analytic formulas of the mobility functions in terms of the state vector $\mathbf{x}$. In the absence of external forces ($\mathbf{F}_1 = \mathbf{F}_2 = \mathbf{0}$), Eq. (3) reduces to a simple expression:

$$\dot{\mathbf{x}} = \begin{bmatrix} \dot{x}_{12} \\ \dot{z}_{12} \\ \dot{z}_C \end{bmatrix} = \begin{bmatrix} 2z_{12}\left(\frac{1}{r_{12}^3} - \frac{1}{R_{12}^3} + 3\frac{x_{12}^2}{R_{12}^5}\right) \\ 2x_{12}\left(\frac{1}{R_{12}^3} - \frac{1}{r_{12}^3} + 12\frac{z_C^2}{R_{12}^5}\right) \\ 6\frac{x_{12}z_{12}z_C}{R_{12}^5}. \end{bmatrix} = \mathcal{G}^{\text{rotlet}}(\mathbf{x}), \tag{4}$$

where $r_{12}^2 = x_{12}^2 + z_{12}^2$ and $R_{12}^2 = x_{12}^2 + 4z_C^2$. Here length and time have been nondimensionalized by the initial height of the system $l_c = z_C^0 = z_C(t = 0)$ and $t_c = \eta l_c^3/\tau$ respectively. Since the rotlets cannot cross the floor, the admissible phase space is bounded by the planes $z_{12} = \pm 2z_C$. As follows from Eq. (4), this constraint is automatically satisfied since $\dot{z}_{12} = \pm 2\dot{z}_C$ when $z_{12} = \pm 2z_C$.

C. Particles with finite radius

When the interparticle or particle-wall distance is of the order of the particle radius, a, the finite-size effects must be included. We account for these effects by using the Rotne-Prager-Yamakawa mobility [42,43] with wall corrections derived by Swan and Brady (see Appendices B and C in Ref. [44]). To obtain an equation in the form of Eq. (3), we rearrange the formulas from Refs. [42–44] in terms of $\mathbf{x} = (x_{12}, z_{12}, z_C)$ and a. As shown in Fig. 3(b), spheres of radius a rotating above a floor translate with a self-induced horizontal velocity v_0, which, to leading order, scales as $(a/h)^4$ (see Ref. [44]), while rotlets do not have a self-induced velocity.

After nondimensionalizing Eq. (3) with $l_c = a$ and $t_c = \eta l_c^3/\tau$, we obtain [45]

$$\dot{\mathbf{x}} = \begin{bmatrix} \dot{x}_{12} \\ \dot{z}_{12} \\ \dot{z}_C \end{bmatrix} = \boldsymbol{\mu}^{U\tau} + B^{-1}\mathbf{M}^{UF} \cdot \begin{bmatrix} \mathbf{F}_1 \\ \mathbf{F}_2 \end{bmatrix}, \tag{5}$$

where $B = \tau/(mga)$ is a dimensionless number that compares the strength of gravity with external torques. In the limit $B \to 0$, the dynamics is mainly dictated by gravity, while when $B \to \infty$ the system is dominated by the torque-driven flows. B can be seen as the ratio of the self-induced velocity due to gravity and the velocity induced by the torque acting on another particle [see Fig. 3(b)]: $B = U_\tau/U_g$ where $U_\tau \sim \tau/\eta a^2$ and $U_g \sim mg/\eta a$. When $B \gg 1$, the upward torque-induced flows can counterbalance or overcome gravity and lead to hydrodynamic bound states. If one assumes a critter-like structure with typical size L, B can also be defined as the ratio of two characteristic times: $B = t_g/t_\tau$ where $t_g = L/U_g \sim L\eta a/mg$ is the characteristic time for a particle to fall across and exit the critter, and $t_\tau \sim L/U_\tau = L\eta a^2/\tau$ is the "overturn" time, i.e., the time for a particle to travel the perimeter of the critter. So a particle is more likely to stay in the critter when $t_\tau \ll t_g$, that is, when $B \gg 1$. Note that the nondimensionalization in Eq. (5) works only for the gravity forces and not for the contact forces introduced in Eq. (2). As explained below, contact forces are just used to prevent particle overlaps near contact, they do not physically matter as long as they remain short-ranged. If one accounts only for gravity, then the force vector on the right-hand side of Eq. (5) simply becomes $[\mathbf{F}_1, \mathbf{F}_2]^T = [0, -1, 0, -1]^T$.

In this work, we want to focus only on the effect of B on the system. Here the goal of repulsive contact forces is to prevent overlaps while having *as little influence as possible* on the dynamics of the system. We therefore chose to use extremely short-range repulsive forces; in practice, we model contact forces with an exponentially decaying repulsive potential of the form [46]

$$U(r) = \begin{cases} U_0\left(1 + \frac{d-r}{b}\right) & \text{if } r < d, \\ U_0 \exp\left(\frac{d-r}{b}\right) & \text{if } r \geqslant d. \end{cases} \tag{6}$$

For particle-particle interactions, r is the center-to-center distance and $d = 2a$. For particle-wall interactions, r is the height of the particle center and $d = a$. The energy scale U_0 and interaction range b control the strength and decay of the potential, respectively. We found that taking $U_0 = \max(3mga/2, \tau/20)$ and $b = 0.025a$ prevents particle-particle and particle-wall overlaps while keeping close contact.

Since spheres cannot overlap each other or the wall, the admissible phase space is bounded by the planes $z_C = a$, $z_{12} = \pm 2(z_C - a)$ and the cylinder $x_{12}^2 + z_{12}^2 = 4a^2$. This region is discretized using a polar cylindrical mesh. The vector field $\mathcal{G}(\mathbf{x})$ [Eq. (3)] is evaluated at the mesh nodes and streamlines, i.e., trajectories, are analyzed.

III. DYNAMICS IN PHASE SPACE

In this section we analyze, numerically and analytically, the trajectories and their stability in phase space. First, we consider the limit $B \to \infty$, where the system is driven only by active flows. Then we study the evolution of the attractors and limit cycles of the system as B varies. We show that

the system undergoes various bifurcations and that periodic orbits can be obtained above a threshold value $B > B^*$.

A. Neutrally stable states: $B \to \infty$

When $B \to \infty$ the particles can be considered as neutrally buoyant, thus the dynamics of the system is driven only by the active flows induced by the external torque. Below we analyze the resulting neutrally stable states and compare the rotlet solutions with the finite sphere solutions.

1. Rotlets

The trajectories of the autonomous dynamical system (4) are highly sensitive to initial conditions. The upper and lower panels in Fig. 4 show an example for two rotlets initially placed at the same height: $z_{12}^0/z_C^0 = 0$. When their initial separation distance is $x_{12}^0/z_C^0 = 2.356$, the rollers exhibit a periodic leapfrog motion, while a small increment, $x_{12}^0/z_C^0 = 2.356 + 0.001 = 2.357$, leads to a diverging trajectory. The critical separation value x_{12}^* for two particles at the same height is given by $\dot{z}_{12} = 0 \Rightarrow 2x_{12}(\frac{1}{R_{12}^3} - \frac{1}{r_{12}^3} + 12\frac{z_C^2}{R_{12}^5}) = 0 \Rightarrow x_{12}^*/z_C^0 = \pm 2.356927998$ [see Fig. 2(b)] [47]. As shown in the lower and upper panels of Fig. 4, when $x_{12} > x_{12}^*$, the rear particle heads downward and the front particle is lifted upward. Such a situation is unstable and leads to a diverging trajectory. When $x_{12} < x_{12}^*$, the rear particle goes up and the front particle goes down, which then leads to a periodic leapfrog motion.

Figure 4 shows the trajectories in phase space (x_{12}, z_{12}, z_C), rescaled by the initial height z_C^0, for various initial separations (x_{12}^0/z_C^0 and z_{12}^0/z_C^0), colored by period of rotation. Contrary to the unbounded case [Eq. (1)], the period of rotation no longer scales with r^3 because of the loss of symmetry in the system, but, as shown in the inset, seems to follow a cubic scaling with the maximum horizontal separation. The phase space exhibits a discontinuous transition between the region of neutrally stable states and unstable trajectories. This discontinuity is purely hydrodynamic in origin and is related to the geometry of the flow field [Fig. 2(b)]: any trajectory that passes through a point with coordinates $(|x_{12}|/z_C^0 < x_{12}^*, 0, z_C/z_C^0 = 1)$ is neutrally stable and periodic; in other words, every time the particles reach the same height their separation distance must be less than x_{12}^* to remain in a periodic hydrodynamic bound state. If the particles never reach the same height, then the trajectory diverges. Note that this system exhibits a phase space similar to the well-known pendulum without friction [48,49], except that the neutrally stable trajectories do not replicate periodically in phase space.

2. Torque-driven spheres

Similarly to a rotlet, a torque-driven sphere, with radius a, above a floor generates a recirculating region whose size depends on h/a [cf. Fig. 1(c) in Ref. [16]]. Figure 5 shows the trajectories of spheres colored by type and rescaled by a. As shown in the inset, at large distances, the behavior of the system is similar to the pair of rotlets: when rescaling lengths by z_C^0 instead of a, the trajectories collapse as in Fig. 4. However, finite-size corrections are perceptible closer to the wall. In addition to the leapfrogging trajectory (orange), a qualitatively different periodic trajectory appears (red) for $z_C < 2a$. The new periodic trajectory corresponds to a vertical oscillation of the translating pair of microrollers. Without the self-induced velocity due to the finite size of the spheres, this trajectory would diverge.

B. A rich phase space for a simple system: $0 < B < \infty$

As seen in the previous section, when $B \to \infty$, all the periodic trajectories are neutrally stable; there is no attractor in the system. In the opposite regime, $B = 0$, the system is exclusively driven by gravity, and there are infinitely many sinks with coordinate $z_C = z_C^{\text{eq}}$, where z_C^{eq} is the equilibrium

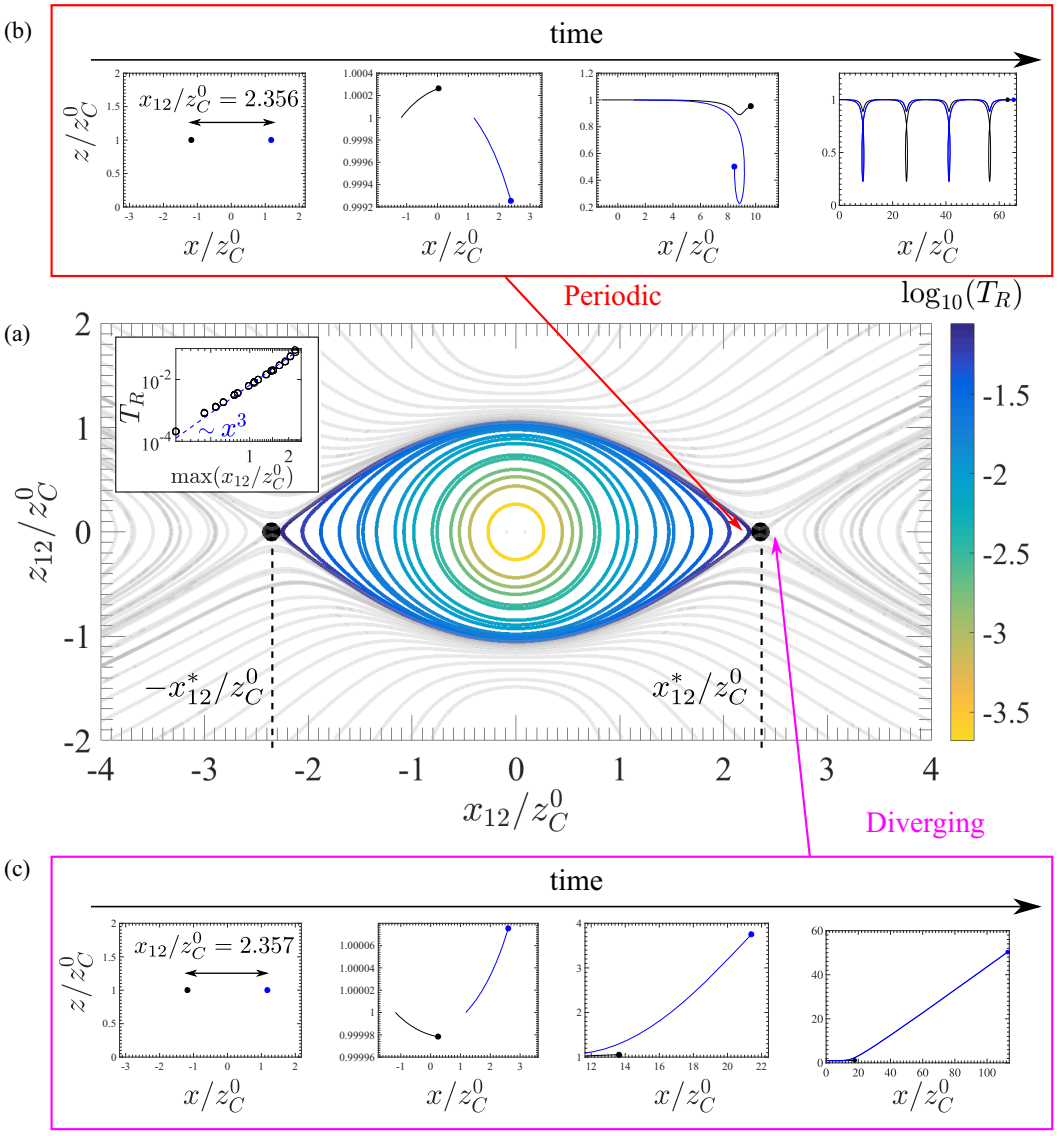

FIG. 4. (a) Trajectories of two rotlets in phase space for $B = \infty$ colored by their period T_R. Gray trajectories diverge. The black circles represent the points ($x_{12}^*/z_C^0 = \pm 2.356927998$, $z_{12}/z_C^0 = 0$, $z_C/z_C^0 = 1$) that lie on the separatrix between neutrally stable and unstable states. Inset: Period of trajectories as a function of the maximum horizontal separation; the dashed blue line is a fit: $T_R \sim \max(x_{12}/z_C^0)^3$. (b), (c) Trajectories in physical space chosen in the vicinity of x_{12}^* ($x_{12}^0/z_C^0 = 2.356$ and $x_{12}^0/z_C^0 = 2.357$, respectively).

value of z_C obtained by balancing gravity and contact forces with the floor. $z_C^{\mathrm{eq}} = a$ for a hard-sphere potential and $z_C^{\mathrm{eq}} \approx 1.1a$ for our repulsive potential (6).

Between these two limits, the landscape of the phase space evolves between six regimes:

(1) $B < 11.1$: two sinks [Fig. 6(a)]
(2) $11.1 < B < 12.8$: one limit cycle + two sinks [Fig. 6(b)]
(3) $12.8 < B < 59.5$: one limit cycle + two spiral sinks [Fig. 6(c)]
(4) $59.5 < B < 77$: one limit cycle + four spiral sinks [Fig. 6(d)]

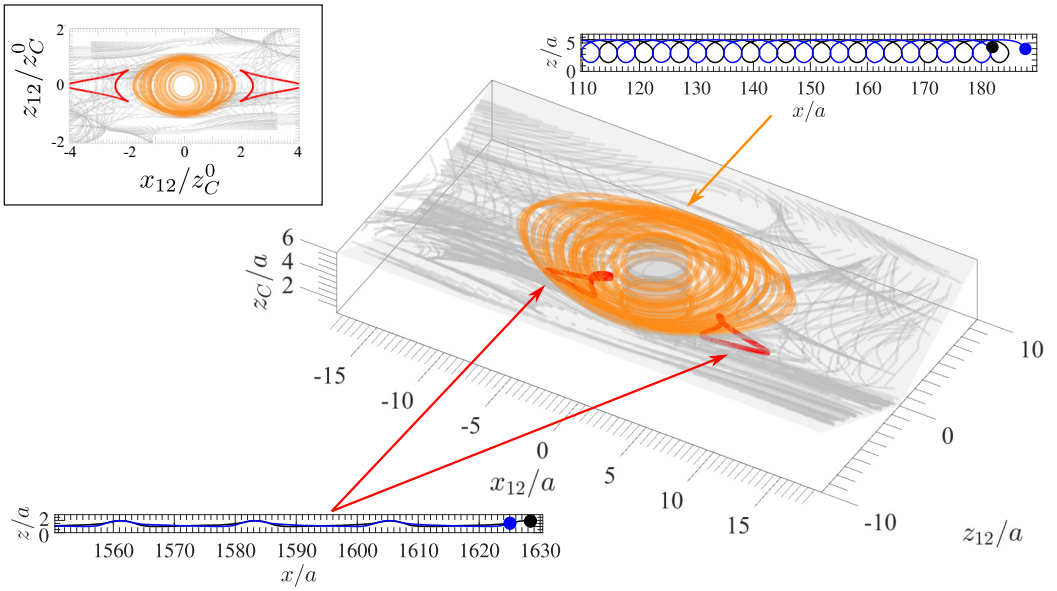

FIG. 5. Trajectories of two spheres of radius a in phase space rescaled by a for $B = \infty$. Trajectories colored by type of periodic motion. Orange trajectories, leapfrog motion; red trajectories, vertical periodic oscillations. Gray trajectories diverge. Inset: Trajectories rescaled by the initial height of the system z_C^0.

(5) $77 < B \leqslant 95.5$: three limit cycles + two spiral sinks [Fig. 6(e)]
(6) $95.5 < B < \infty$: one limit cycle + two spiral sinks [Fig. 6(f)]

Figure 6 shows the phase space for the six regimes. Trajectories are colored according to the basin of attraction to which they belong.

Below we identify the fixed points and limit cycles of these regimes and analyze their evolution as B varies.

1. Leapfrog (LF) orbits

Unlike neutrally buoyant particles, the existence of leapfrog (LF) trajectories depends not only on the initial particle positions but also on the competition between gravity and torque-driven flows. This competition defines a critical value, B^*, above which active flows overcome the effect of gravity and a leapfrog trajectory appears [see Fig. 3(b)]. This discontinuous transition is shown in Fig. 6(b) as the appearance of the orange trajectories that converge to the leapfrog limit cycle (thick black line). The leapfrog trajectory is a unique limit cycle that appears at $B^* = 11.7$ and whose basin of attraction increases with B. Figure 7 shows the evolution of the leapfrog trajectories as B increases. When $B = B^* = 11.7$, active flows are just strong enough to overcome the delaying effect of gravity [cf. Fig. 3(b)], as shown by the shape of the trajectories. As B increases, the period of the orbit decreases and the motion becomes circular.

The leapfrog orbit is reminiscent of the periodic treadmilling motion followed by the microrollers that self-assemble into critter (Fig. 1). Therefore, for a given particle size and mass, these results indicate that critters can appear only above a threshold value of the external torque, which is also suggested by our previous experimental observations and numerical simulations [16,46].

Various parameters can be changed in the experiments to vary B, for example, particle size, magnitude of the external torque, and particle mass. We will explore these directions in the near future to better understand how the critter state emerges and how it can be controlled.

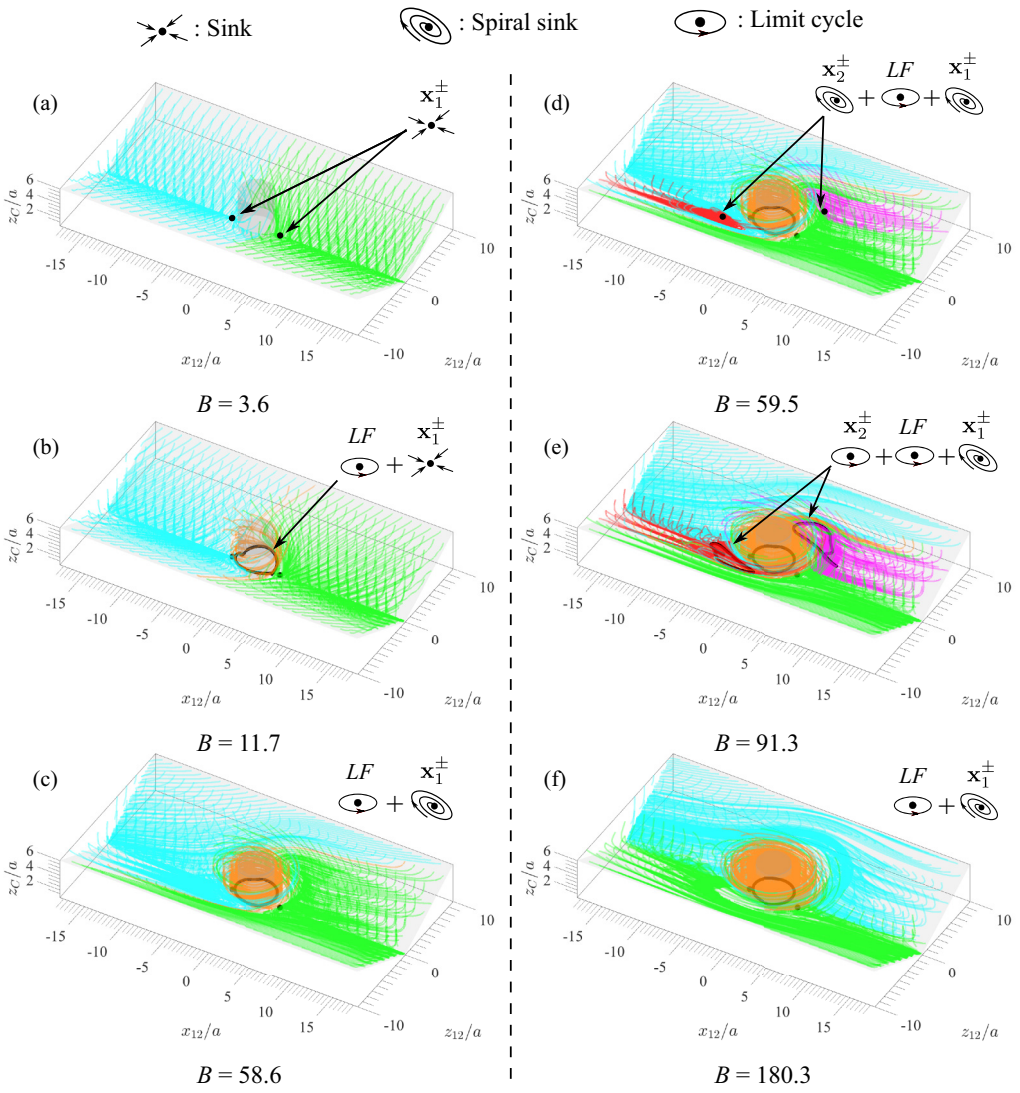

FIG. 6. Trajectories of two particles in phase space for finite values of B. Black circle, fixed points (sinks); black trajectories, limit cycles. Each color corresponds to different basin of attraction: blue and green trajectories are attracted to the fixed points $\mathbf{x}_1^{\pm}$; orange trajectories converge to the leapfrog (LF) limit cycle; red and magenta trajectories are attracted to the fixed points $\mathbf{x}_2^{\pm}$, which undergo a Hopf bifurcation at $B = 77$.

2. Surviving sinks $\mathbf{x}_1^{\pm}$

Two symmetric sinks survive for all values of $B \in [0; \infty[$, these are indicated in Fig. 6 by the black circles close to the cylinder delimiting the excluded volume region. As shown in Fig. 8(c), these fixed points, with coordinates $\mathbf{x}_1^{\pm} = (\pm 2.95a, 0, z_C^{\mathrm{eq}})$, correspond to a stable state where the particles are sedimented near the floor and translate at the same height with a constant separation distance ($x_{12} = \pm 2.95a$). To study the stability of these fixed points, we linearize Eq. (3) about $\mathbf{x}_1^{\pm}$:

$$\delta\dot{\mathbf{x}}_1 = \boldsymbol{\nabla}\mathcal{G}(\mathbf{x}_1^{\pm}) \cdot \delta\mathbf{x}_1, \tag{7}$$

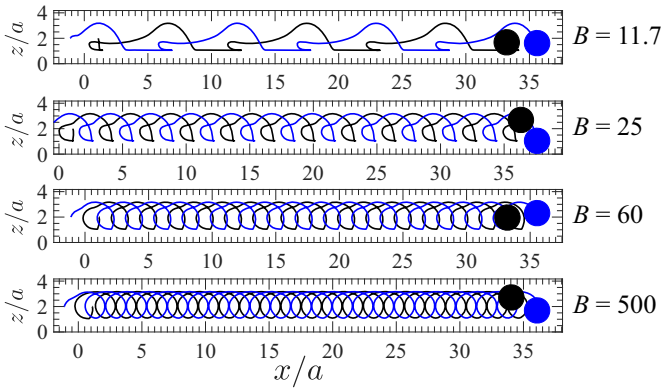

FIG. 7. Leapfrog trajectories for $B = 11.7 - 500$, where $B^* = 11.7$ is the critical value.

where $\delta\mathbf{x}_1 = \mathbf{x} - \mathbf{x}_1^{\pm}$. Note that $\nabla\mathcal{G}(\mathbf{x}_1^{\pm})$ is expressed *analytically* as a function of B and the contact force parameters. As mentioned in Sec. II C, the contact force parameters are chosen to minimize their influence on the trajectories of the system. The three eigenvalues and eigenvectors of $\nabla\mathcal{G}(\mathbf{x}_1^{\pm})$ are then computed.

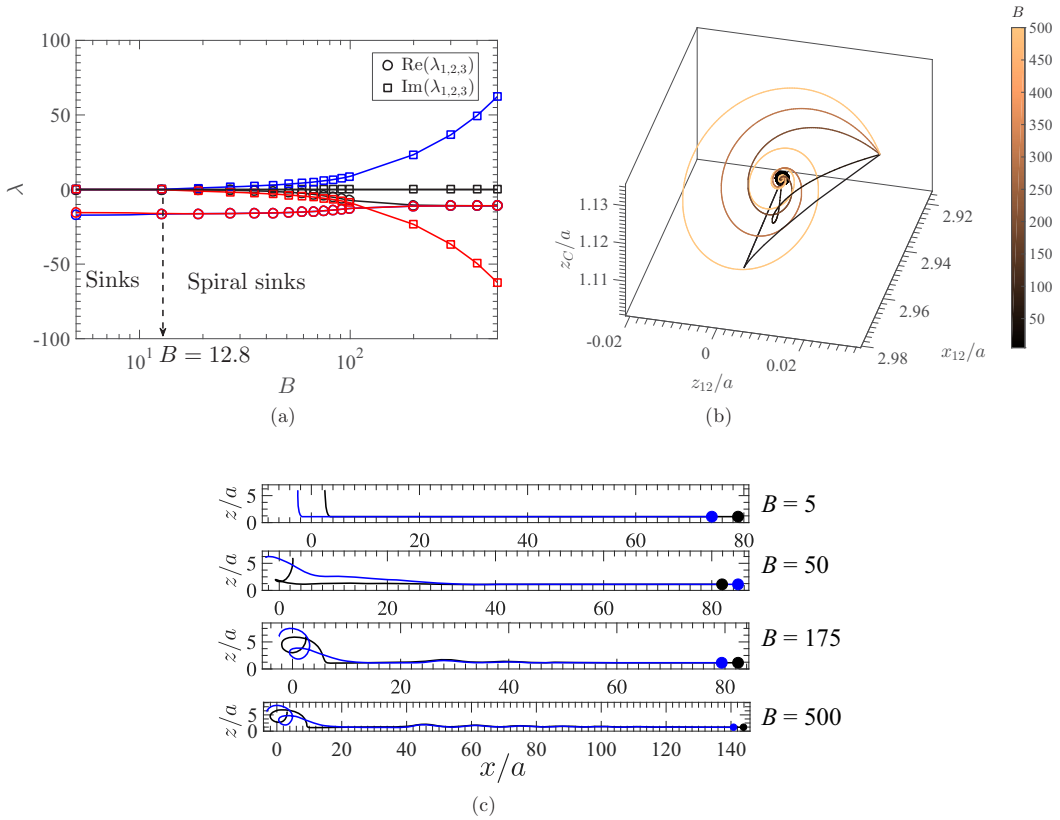

FIG. 8. Characterization of the surviving sinks $\mathbf{x}_1^{\pm}$. (a) Eigenvalues $\lambda_{1,2,3}$ of $\nabla\mathcal{G}(\mathbf{x}_1^{\pm})$ vs B (cf. Eq. 7). Each color represents a different eigenvalue, (b) Linearized trajectories in the vicinity of $\mathbf{x}_1^{\pm}$ colored by the value of B. Black circle: position of $\mathbf{x}_1^{\pm}$, and (c) Examples of trajectories converging to $\mathbf{x}_1^{\pm}$ in physical space.

Figure 8(a) shows the real and imaginary part of each eigenvalues for $B = 1 - 500$. First, we note that all eigenvalues have negative real parts, confirming that this is a stable fixed point. We also observe a bifurcation from zero to nonzero (conjugate) imaginary parts at $B = 12.8$, where $\mathbf{x}_1^{\pm}$ becomes a spiral sink. Figure 8(b) shows the corresponding linearized trajectories in phase space in the vicinity of $\mathbf{x}_1^{\pm}$ for $B = 1 - 500$. Below the threshold value $B = 12.8$, the system relaxes exponentially to the fixed point. As B increases, the active flows get stronger and the trajectories oscillate towards $\mathbf{x}_1^{\pm}$ [see third and fourth panels in Fig. 8(c)]. Note that x_{12} is the slowest degree of freedom, which is intuitive since gravity tends to stabilize z_{12} and z_C first. Once z_{12} and z_C are close to their equilibrium value, the only nonzero component of the vector field is the first component, $\mathcal{G}_x$, along the x_{12} axis. $\mathcal{G}_x(x_{12}, 0, z_C^{\mathrm{eq}})$ is very small and has only one zero at $x_{12} = \pm C$. Therefore, when a pair of particle settles to the floor, i.e., when $z_{12} \to 0$ and $z_C \to z_C^{\mathrm{eq}}$, it moves slowly in phase space along the x_{12} axis towards $\mathbf{x}_1^{\pm}$ [see Figs. 8(b) and 8(c)]. Thus, compared to the other fixed points, $\mathbf{x}_1^{\pm}$ has the largest basin of attraction.

3. Hopf bifurcation at $\mathbf{x}_2^{\pm}$

When $B = 59.5$, two additional symmetric spiral sinks, $\mathbf{x}_2^{\pm}$, appear in the system. In this situation, the active flows are strong enough to counterbalance gravity and maintain a stable configuration where one particle, at the front, is lifted by the other one that is closer to the floor [see Fig. 3(b) and

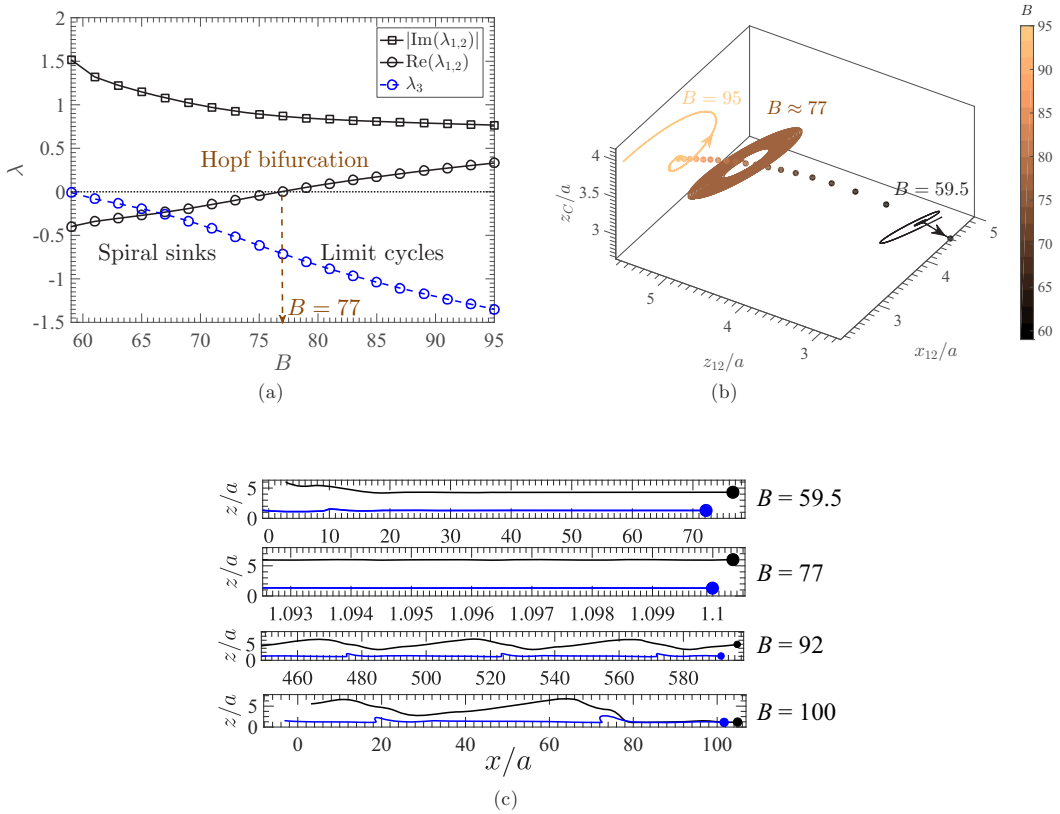

FIG. 9. Characterization of the Hopf bifurcation at the fixed points $\mathbf{x}_2^{\pm}$. (a) Eigenvalues $\lambda_{1,2,3}$ of $\nabla\mathcal{G}(\mathbf{x}_2^{\pm})$ vs B. Black lines: conjugate complex eigenvalues $\lambda_{1,2}$. Blue line: real eigenvalue λ_3, (b) Linearized trajectories in the vicinity of $\mathbf{x}_2^{\pm}$ colored by the value of B. Circles: position of $\mathbf{x}_2^{\pm}$, and (c) Examples of trajectories in the vicinity of $\mathbf{x}_2^{\pm}$ in physical space.

first panel in Fig. 9(c)]. But as B increases, gravity is weaker and loses its role of stabilizer, which leads to the appearance of a limit cycle at $B = 77$. As B increases further, the limit cycle grows and disappears for $B > 95.5$ [see Fig. 9(c)]. We carry out a linear stability analysis of the system in the vicinity of $\mathbf{x}_2^{\pm}$. The eigenvalues of $\nabla\mathcal{G}(\mathbf{x}_2^{\pm})$, plotted in Fig. 9(a), show that the linearized system undergoes a Hopf bifurcation at $B = 77$: the real part of the complex conjugate eigenvalues becomes positive, which corresponds to the birth of a limit cycle in the nonlinear case. Linearized trajectories in the vicinity of $\mathbf{x}_2^{\pm}$ are shown in Fig. 9(b). Contrary to $\mathbf{x}_1^{\pm}$, the coordinates of $\mathbf{x}_2^{\pm}$ change with B. In particular the height of the center of mass z_C increases from $2.68a$ to $3.92a$, and the vertical separation z_{12} increases from $2.75a$ to $5.17a$. As illustrated by the first and second panel of Fig. 9(c), when B increases, active flows become stronger compared to gravity and therefore increase the equilibrium height of the front particle, while the rear particle remains approximately at a constant height of $1.3a$.

It is important to mention that these trajectories are purely hydrodynamic in origin. The particles never touch each other or the wall; thus our results do not depend on the details of the contact forces.

IV. CONCLUSIONS AND DISCUSSION

We have analyzed the phase space of a simple dynamical system: two coplanar microrollers above a no-slip boundary. We use this elementary model as the starting point to identify the conditions for the spontaneous self-assembly of microrollers into stable motile structures. Despite its apparent simplicity, we find that this system exhibits a wide variety of complex behaviors that are controlled by a dimensionless parameter B, which compares the external torque to gravity. In the limit $B \to \infty$, active particles are neutrally buoyant and the phase space is divided into two regions: a region with neutrally stable periodic leapfrog trajectories, and a region of diverging trajectories. Leapfrog trajectories can be obtained only when particle reach the same height with a separation distance below a threshold value x_{12}^*.

For finite values of B, the system exhibits various attractors whose existence and stability depend on B. In particular, the leapfrog motion exists only above a critical value B^*, for which active flows can overcome gravity. This leapfrog motion is a unique limit cycle whose basin of attraction increases with B. Even though our hydrodynamic interactions are not fully resolved and overestimate particle mobilities, we conjecture that more resolved solutions would not affect the existence of this threshold value, but only shift B^* to a higher value. Leapfrogging motion of pairs of particles has been observed in previous experiments with dilute suspensions of microrollers [23] and is thought to be at the origin of the self-assembly into critters.

We have also discovered the existence of an another stable state at $B = 59.5$, where a particle at the rear lifts another particle up at the front. This fixed point undergoes a Hopf bifurcation at $B = 77$ and then disappears at $B = 95.5$. The existence of this fixed point is also of importance since, before self-assembling into critters, microrollers at the front are lifted up the floor by the others at the rear.

Given its simplicity and rich behavior, this system could be used as an introduction to dynamical systems and fluid dynamics in a textbook at the (under-)graduate level. The visual nature of the results and their strong connection to experiments, simulations, and current state-of-the-art research provide a potentially useful tool for science outreach. A model experiment can be implemented with two magnetic particles driven by a coil in a small chamber. However, one needs to make sure that interparticle magnetic interactions remain weak compared to hydrodynamic forces (small Mason number). This can be achieved with the particles used in our prior work [16] or with polystyrene Janus particles half-coated with a very thin layer of nickel ($\sim$10 nm) [50].

So far we have focused only on the limit of large Péclet number (Pe $\to \infty$), where thermal diffusion can be neglected compared to convection. At finite Pe, two dimensionless numbers can be defined in the system: the Péclet number, $\mathrm{Pe} = Ua/D = U\eta a^2/k_BT = \tau/k_BT$, where $U = \tau/\eta a^2$ is a typical advective velocity induced by the external torque, k_B is the Boltzmann constant, and T the solvent temperature, and the gravitational height h_g that balances gravity with thermal diffusion:

$h_g/a = kT/mga$ (note that Pe $\times$ $h_g/a = \tau/mga = B$). At finite Pe, the motion of the microrollers is given by the overdamped Langevin equations, which require specific time-integration scheme [51–54]. Using our computational tools [46], we will study the effect of Pe and h_g on the trajectories in phase space in the near future. In particular, it will be interesting to evaluate the robustness of the fixed points and limit cycles versus noise.

In this work we have chosen to focus only on two coplanar particles for two reasons. First, translational invariance permits a description of the system with only three degrees of freedom. The three-dimensional phase space can therefore be visualized and analyzed easily. Second, we are mostly interested in the height dynamics of the system and not in the transverse motion, which we have already analyzed in previous work [16,24]. Considering transverse motion along the y direction adds one more equation in Eq. (3) and adds one more dimension to the phase space.

In our large-scale simulations and experiments [16], the critters are made of hundreds or thousands of microrollers. The number of degrees of freedom, i.e., the dimension of the phase space, for N particles in the xz plane is $N(N-1)+1$. Detecting and identifying all the fixed points and limit cycles in such high dimensions is not tractable nor is it useful. Instead of adding more and more particles to our dynamical system (3), we plan to study microroller suspensions and self-assembly in the continuum limit. We will rely on the formalism developed in Ref. [23] to derive a conservation equation for the number density of microrollers, where the advective fluxes are evaluated using convolution integrals with a hydrodynamic interaction kernel and the number density everywhere in the domain. These hydrodynamic interaction kernels are directly obtained from the mobility functions [41–44] and therefore account for the finite particle size. Solving the conservation equation numerically (e.g., using a high order finite-volume scheme), we will determine the influence of B on the dynamics and on the steady-state structures of the system in two and three dimensions. Once a steady-state structure is found, its stability will be analyzed numerically and analytically. As shown by our previous work [16], critters can be used for guided particle transport, flow generation, and mixing in microfluidic systems. We will use these theoretical results together with large-scale numerical simulations to optimize the critters generated in experiments.

ACKNOWLEDGMENTS

I thank Michelle Driscoll and Aleksandar Donev for their critical reading of the manuscript and Paul Chaikin and Daniel Abrams for insightful discussions on this work. This work was supported primarily by the Materials Research Science and Engineering Center (MRSEC) program of the National Science Foundation under Award Number DMR-1420073. Additional support was provided by the Division of Chemical, Bioengineering, Environmental and Transport Systems program of the National Science Foundation under award CBET-1706562.

[1] E. Lauga and T. R. Powers, The hydrodynamics of swimming microorganisms, Rep. Prog. Phys. **72**, 096601 (2009).

[2] R. Golestanian, J. M. Yeomans, and N. Uchida, Hydrodynamic synchronization at low Reynolds number, Soft Matter **7**, 3074 (2011).

[3] T. Vicsek and A. Zafeiris, Collective motion, Phys. Rep. **517**, 71 (2012).

[4] M. C. Marchetti, J. F. Joanny, S. Ramaswamy, T. B. Liverpool, J. Prost, M. Rao, and R. A. Simha, Hydrodynamics of soft active matter, Rev. Mod. Phys. **85**, 1143 (2013).

[5] C. Bechinger, R. Di Leonardo, H. Löwen, C. Reichhardt, G. Volpe, and G. Volpe, Active particles in complex and crowded environments, Rev. Mod. Phys. **88**, 045006 (2016).

[6] X.-L. Wu and A. Libchaber, Particle Diffusion in a Quasi-Two-Dimensional Bacterial Bath, Phys. Rev. Lett. **84**, 3017 (2000).

[7] H. H. Wensink, J. Dunkel, S. Heidenreich, K. Drescher, R. E. Goldstein, H. Löwen, and J. M. Yeomans, Meso-scale turbulence in living fluids, Proc. Natl. Acad. Sci. USA **109**, 14308 (2012).
[8] J. Dunkel, S. Heidenreich, K. Drescher, H. H. Wensink, M. Bär, and R. E. Goldstein, Fluid Dynamics of Bacterial Turbulence, Phys. Rev. Lett. **110**, 228102 (2013).
[9] A. Creppy, O. Praud, X. Druart, P. L. Kohnke, and F. Plouraboué, Turbulence of swarming sperm, Phys. Rev. E **92**, 032722 (2015).
[10] D. R. Brumley, K. Y. Wan, M. Polin, and R. E. Goldstein, Flagellar synchronization through direct hydrodynamic interactions, Elife **3**, e02750 (2014).
[11] P. Fischer and A. Ghosh, Magnetically actuated propulsion at low Reynolds numbers: Towards nanoscale control, Nanoscale **3**, 557 (2011).
[12] N. Bruot and P. Cicuta, Realizing the physics of motile cilia synchronization with driven colloids, Annu. Rev. Condens. Matter Phys. **7**, 323 (2016).
[13] A. Snezhko, Complex collective dynamics of active torque-driven colloids at interfaces, Curr. Opin. Colloid Interface Sci. **21**, 65 (2016).
[14] A. Aubret, S. Ramananarivo, and J. Palacci, Eppur si muove, and yet it moves: Patchy (phoretic) swimmers, Curr. Opin. Colloid Interface Sci. **30**, 81 (2017).
[15] M. Driscoll and B. Delmotte, Leveraging collective effects in externally driven colloidal suspensions: Experiments and simulations, Curr. Opin. Colloid Interface Sci. **40**, 42 (2019).
[16] M. Driscoll, B. Delmotte, M. Youssef, S. Sacanna, A. Donev, and P. Chaikin, Unstable fronts and motile structures formed by microrollers, Nat. Phys. **13**, 375 (2017).
[17] F. Martínez-Pedrero and P. Tierno, Advances in colloidal manipulation and transport via hydrodynamic interactions, J. Colloid Interface Sci. **519**, 296 (2018).
[18] P. Tierno, R. Golestanian, I. Pagonabarraga, and F. Sagués, Controlled Swimming in Confined Fluids of Magnetically Actuated Colloidal Rotors, Phys. Rev. Lett. **101**, 218304 (2008).
[19] A. Bricard, J.-B. Caussin, N. Desreumaux, O. Dauchot, and D. Bartolo, Emergence of macroscopic directed motion in populations of motile colloids, Nature (London) **503**, 95 (2013).
[20] G. Kokot, S. Das, R. G. Winkler, G. Gompper, I. S. Aranson, and A. Snezhko, Active turbulence in a gas of self-assembled spinners, Proc. Natl. Acad. Sci. USA **114**, 12870 (2017).
[21] K. Yeo, E. Lushi, and P. M. Vlahovska, Collective Dynamics in a Binary Mixture of Hydrodynamically Coupled Microrotors, Phys. Rev. Lett. **114**, 188301 (2015).
[22] K. Yeo, E. Lushi, and P. M. Vlahovska, Dynamics of inert spheres in active suspensions of micro-rotors, Soft Matter **12**, 5645 (2016).
[23] B. Delmotte, M. Driscoll, P. Chaikin, and A. Donev, Hydrodynamic shocks in microroller suspensions, Phys. Rev. Fluids **2**, 092301(R) (2017).
[24] B. Delmotte, A. Donev, M. Driscoll, and P. Chaikin, Minimal model for a hydrodynamic fingering instability in microroller suspensions, Phys. Rev. Fluids **2**, 114301 (2017).
[25] M. Mirzakhanloo, M. A. Jalali, and M.-R. Alam, Hydrodynamic choreographies of microswimmers, Sci. Rep. **8**, 3670 (2018).
[26] H. Gadêlha, E. A. Gaffney, D. J. Smith, and J. C. Kirkman-Brown, Nonlinear instability in flagellar dynamics: A novel modulation mechanism in sperm migration? J. R. Soc., Interface **7**, 1689 (2010).
[27] R. Di Leonardo, D. Dell'Arciprete, L. Angelani, and V. Iebba, Swimming with an Image, Phys. Rev. Lett. **106**, 038101 (2011).
[28] H. Shum and E. A. Gaffney, Hydrodynamic analysis of flagellated bacteria swimming near one and between two no-slip plane boundaries, Phys. Rev. E **91**, 033012 (2015).
[29] S. E. Spagnolie and E. Lauga, Hydrodynamics of self-propulsion near a boundary: Predictions and accuracy of far-field approximations, J. Fluid Mech. **700**, 105 (2012).
[30] V. Kantsler, J. Dunkel, M. Polin, and R. E. Goldstein, Ciliary contact interactions dominate surface scattering of swimming eukaryotes, Proc. Natl. Acad. Sci. USA. **110**, 1187 (2013).
[31] E. Lushi, V. Kantsler, and R. E. Goldstein, Scattering of biflagellate microswimmers from surfaces, Phys. Rev. E **96**, 023102 (2017).
[32] D. G. Crowdy and Y. Or, Two-dimensional point singularity model of a low-Reynolds-number swimmer near a wall, Phys. Rev. E **81**, 036313 (2010).

[33] D. Crowdy and O. Samson, Hydrodynamic bound states of a low-Reynolds-number swimmer near a gap in a wall, J. Fluid Mech. **667**, 309 (2011).
[34] D. Crowdy, Treadmilling swimmers near a no-slip wall at low Reynolds number, Intl. J. Non-Linear Mechanics **46**, 577 (2011).
[35] A. M. J. Davis and D. G. Crowdy, Stresslet asymptotics for a treadmilling swimmer near a two-dimensional corner: Hydrodynamic bound states, Proc. R. Soc. A **468**, 3765 (2012).
[36] F. Martinez-Pedrero, E. Navarro-Argemí, A. Ortiz-Ambriz, I. Pagonabarraga, and P. Tierno, Emergent hydrodynamic bound states between magnetically powered micropropellers, Sci. Adv. **4**, eaap9379 (2018).
[37] M. Leoni and T. B. Liverpool, Dynamics and interactions of active rotors, Europhys. Lett. (EPL) **92**, 64004 (2011).
[38] Y. Fily, A. Baskaran, and M. Cristina Marchetti, Cooperative self-propulsion of active and passive rotors, Soft Matter **8**, 3002 (2012).
[39] E. Lushi and P. M. Vlahovska, Periodic and chaotic orbits of plane-confined micro-rotors in creeping flows, J. Nonlinear Sci. **25**, 1111 (2015).
[40] F. Balboa Usabiaga, B. Kallemov, B. Delmotte, A. P. S. Bhalla, B. E. Griffith, and A. Donev, Hydrodynamics of suspensions of passive and active rigid particles: A rigid multiblob approach, Commun. Appl. Math. Comp. Sci. **11**, 217 (2016).
[41] J. R. Blake and A. T. Chwang, Fundamental singularities of viscous flow, J. Eng. Math. **8**, 23 (1974).
[42] J. Rotne and S. Prager, Variational treatment of hydrodynamic interaction in polymers, J. Chem. Phys. **50**, 4831 (1969).
[43] H. Yamakawa, Transport properties of polymer chains in dilute solution: Hydrodynamic interaction, J. Chem. Phys. **53**, 436 (1970).
[44] J. W. Swan and J. F. Brady, Simulation of hydrodynamically interacting particles near a no-slip boundary, Phys. Fluids (1994–present) **19**, 113306 (2007).
[45] We could have chosen $l_c = z_C^0$ but, as shown below, the phase space is simpler to visualize with $l_c = a$.
[46] F. B. Usabiaga, B. Delmotte, and A. Donev, Brownian dynamics of confined suspensions of active microrollers, J. Chem. Phys. **146**, 134104 (2017), Software available at https://github.com/stochasticHydroTools/RigidMultiblobsWall.
[47] Note that $\dot{x}_{12} = 0$ and $\dot{z}_C = 0$ when $z_{12} = 0$. It is also worth mentioning that $x_{12} = 0$ is a singular critical point.
[48] G. G. Stokes, *On the Effect of the Internal Friction of Fluids on the Motion of Pendulums*, Vol. 9 (Pitt Press, Cambridge, 1851).
[49] G. L. Baker and J. A. Blackburn, *The Pendulum: A Case Study in Physics* (Oxford University Press, Oxford, 2005).
[50] W. Fei, M. M. Driscoll, P. M. Chaikin, and K. J. M. Bishop, Magneto-capillary dynamics of amphiphilic Janus particles at curved liquid interfaces, Soft Matter **14**, 4661 (2018).
[51] S. Delong, F. B. Usabiaga, R. Delgado-Buscalioni, B. E. Griffith, and A. Donev, Brownian dynamics without Green's functions, J. Chem. Phys. **140**, 134110 (2014).
[52] S. Delong, F. B. Usabiaga, and A. Donev, Brownian dynamics of confined rigid bodies, J. Chem. Phys. **143**, 144107 (2015).
[53] B. Delmotte and E. E. Keaveny, Simulating Brownian suspensions with fluctuating hydrodynamics, J. Chem. Phys. **143**, 244109 (2015).
[54] B. Sprinkle, F. Balboa Usabiaga, N. A. Patankar, and A. Donev, Large scale Brownian dynamics of confined suspensions of rigid particles, J. Chem. Phys. **147**, 244103 (2017).